Life Cycle Characteristics of MCSs in Middle East China Tracked by Geostationary Satellite and Precipitation Estimates

YUFEI AI

Laboratory for Climate and Ocean–Atmosphere Studies, Department of Atmospheric and Oceanic Sciences, School of Physics, Peking University, Beijing, China, and Cooperative Institute for Meteorological Satellite Studies, University of Wisconsin–Madison, Madison, Wisconsin

WANBIAO LI AND ZHIYONG MENG

Laboratory for Climate and Ocean–Atmosphere Studies, Department of Atmospheric and Oceanic Sciences, School of Physics, Peking University, Beijing, China

JUN LI

Cooperative Institute for Meteorological Satellite Studies, University of Wisconsin–Madison, Madison, Wisconsin

(Manuscript received 19 May 2015, in final form 4 April 2016)

ABSTRACT

By combining high temporal and spatial resolution *Multifunctional Transport Satellite-1R* (*MTSAT-1R*) infrared (IR) images and precipitation data from the Climate Prediction Center morphing technique (CMORPH), this study tracked mesoscale convective systems (MCSs) from May to August in 2008 and 2009 in the middle of east China with an automatic tracking algorithm based on an areal overlapping methodology. This methodology is adjusted to include those MCSs with a relative weak intensity before formation. The unique advantage of combining high temporal and spatial resolution geostationary satellite brightness temperature images and the precipitation measurements for tracking MCSs is that the cloud-top height along with the coverage and the precipitation intensity can be well identified. Results showed that the MCSs formed most frequently in the southwest Henan Province and at the border of four provinces—Shandong, Henan, Anhui, and Jiangsu—which is east of the convergence zone near the terrain's edge. Locations of the highest cloud tops and of the heaviest precipitation rates did not always match. In addition, the MCSs in the study region tended to first reach the maximum precipitation rate, followed soon by the minimum brightness temperature, then the maximum associated precipitation area, and finally the maximum in system area.

1. Introduction

Mesoscale convective systems (MCSs) are severe weather systems that may cause heavy rains, lightning, wind gusts, floods, and hail. They lead to most of the heavy precipitation in east China resulting in flooding events, such as over the Huaihe basin in 1991 and over the Yangtze River basin in 1998 (Bei et al. 2002; Sun et al. 2010; Zheng et al. 2013). MCSs are usually composed of a convective core, stratiform anvil, and nonprecipitating cirriform cloudiness.

The convective core is the place in which heavy rainfall occurs with a typical scale of 10–100 km. The stratiform anvil with lighter precipitation, as well as the nonprecipitating cirriform cloudiness, are both typically on a scale of 100–1000 km (Houze 2004). MCSs over the tropics and midlatitudes both occur frequently in the afternoon and develop quickly with intense rain and winds (Machado et al. 1998; Pope et al. 2008). In east China, however, afternoon is not the only peak for MCSs formation but another peak in early morning is also observed by previous studies (Zheng et al. 2008, 2013; Meng et al. 2013). The physical basis for MCS forecasting is based on its evolution, which follows typical patterns of behavior depending on the general features of the MCS life cycle (Vila et al. 2008). Therefore, knowing the life cycle

---

Corresponding author address: Wanbiao Li, Department of Atmospheric and Oceanic Sciences, School of Physics, Peking University, 209 Chengfu Rd., Beijing 100871, China.
E-mail: lwb@pku.edu.cn

characteristics of MCSs in a certain area is quite important for making forecast decisions.

Remote sensing data including both satellite and radar imagery have long been used to perform climatological studies on MCSs (Maddox 1980; Laing and Fritsch 1997; Mathon and Laurent 2001; Zheng et al. 2008; Meng et al. 2013; Xu 2013). Ground-based radar at a fixed location is an important instrument that can estimate precipitation from MCSs within its detecting range based on the measured radar reflectivity. However, the scanning strategy for an S-band ground-based radar (10-cm wavelength) has a detection range of 460 km horizontally for radar reflectivity and 230 km for radial velocity and 15 km vertically. These detection ranges are too small to detect the life cycle of an MCS given its typical long time scale. Compared to radar, geostationary (GEO) satellite products can reveal cloud-top evolution before precipitation starts with a larger coverage, and low earth orbit (LEO) satellites are able to detect the precipitation structure of MCSs through specific channels with fine time and spatial resolution, covering various stages of MCSs, revealing important information about the cloud top, cloud structure, and precipitation. Generally, infrared (IR) radiance images are converted to brightness temperature (BT) to identify deep convection, characterized by high cloud tops and low BTs. The strong contrast between the warmer background and colder cloud tops is the basis for identifying and tracking MCSs. Most earlier research used only satellite images from the visible and IR bands to track MCSs. For example, IR images were used by Machado et al. (1998) to track the life cycle of MCSs over the Americas, by Mathon and Laurent (2001) over Africa, and by Zheng et al. (2008) to study the spatial and diurnal distribution of MCSs in China region over a 10-yr period from 1996 to 2006. Schröder et al. (2009) developed an automatic algorithm for tracking MCSs via GEO satellites based on an areal overlapping method, which assumes that an MCS does not vary too much in area and position between two successive images. Although these studies investigated cloud-top features of MCSs, they did not track the precipitation for a single MCS, revealing little information on the evolution of precipitation in real time.

Precipitation, one of the most important parameters in analyzing climate and weather, is usually observed via ground rain gauges, radar, and satellites. Studies show that precipitation from MCSs accounted for most of the total rainfall (Meisner and Arkin 1987). MCS studies often use precipitation to describe the convective intensity (Xu and Zipser 2011; Feng et al. 2012; Goyens et al. 2012; Xu 2013). Short-time variations in MCS precipitation are crucial in the forecasting and nowcasting of

MCS weather (Migliorini et al. 2011; Kolios and Feidas 2013). Since MCSs have similar structures, cloud-top features alone cannot distinguish between different precipitation structures and whether hail, tornadoes, or gusty winds occur under the high anvil of a large area. It is important to perform a survey of MCSs using both the satellite imagery and precipitation data to study MCS life cycle patterns from the perspective of both clouds and precipitation. Yuan and Houze (2010) used multisatellite products from the Moderate Resolution Imaging Spectroradiometer (MODIS) and Advanced Microwave Scanning Radiometer for Earth Observing System (AMSR-E) to identify tropical MCSs and analyze their structures. They found that some MCSs with separate convective cores are connected both in cloud tops and rain areas. Goyens et al. (2012) combined IR satellite imagery and Tropical Rainfall Measuring Mission (TRMM) precipitation products focusing on MCSs in the Sahel, showing the quantitative relationships between cloud parameters and precipitation estimates. Feng et al. (2012) analyzed MCSs over the central United States with a hybrid of GOES satellite and Next Generation Weather Radar (NEXRAD) reflectivity data, and found the maximum convective system size correlates with lifetime. They discovered the close relationship between MCS clouds and precipitation, completing the knowledge on the life cycles of satellite-tracked MCSs in some particular regions. Although climatological studies on the general features of MCSs have been conducted based on satellite imagery and radar mosaic images for different MCS structures (Meng et al. 2013; Zheng et al. 2008, 2013), this kind of information has not been examined in east China. As in the United States, MCSs are a common disastrous weather phenomenon in east China from early spring to late autumn (Machado et al. 1998; Zheng et al. 2008). The thermodynamic conditions [e.g., convective available potential energy (CAPE) and convection inhibition (CIN)] and dynamic conditions (e.g., environmental winds) are different between China and the United States based on previous research (Dai 2001; Zhang 2003; Tian et al. 2005). Studies have also shown weaker averaged vertical wind shear and moister air in China than in the United States (Laing and Fritsch 2000). The diurnal cycle of thermodynamic parameters also have different patterns in China (Dai 2001). As LeMone et al. (1998) pointed out, weaker shear tends to result in more nonlinear MCSs and larger humidity contributes to longer life durations. Similar to the United States, China also has terrain conditions, which have impact on the horizontal convergence, resulting in its specific pattern of MCS spatial distribution.

Although studies on MCS tracking and analysis have been conducted over China, most studies either used satellite data, which reflect the characteristics of

cloud-top height (CTH) and coverage, or radar measurements, which indicate the precipitation intensity. But often the CTH and precipitation intensity are not well correlated, especially over China; for example, warm clouds with relatively high brightness temperatures in satellite measurements often bring heavy rainfall in summer over China (Yu et al. 2010). To reflect both CTH and precipitation intensity characteristics, the high temporal (better than 1 h) and spatial (better than 5 km at nadir) resolution geostationary satellite infrared brightness temperature images and the collocated high temporal (30 min) and spatial (8 km) resolution Climate Prediction Center morphing technique (CMORPH) data are combined to study MCSs over China in this study. A research method using both satellite imagery and precipitation data has not been applied to track MCSs over China. Precipitation data were used in previous studies of MCSs, but the measurements were either of accumulated rainfall or of near-real-time precipitation derived from TRMM, which does not have enough sampling either spatially or temporally. The real-time precipitation data from CMORPH has the unique advantage of high temporal and spatial resolution and global coverage that, along with the high-resolution geostationary satellite IR data, is ideal for studying the detailed evolution of precipitation and the relationship between precipitation intensity and CTH of MCSs. In addition, since satellite imagery measuring the cloud-top radiation has the potential to detect convective clouds before precipitation starts, the methodology has been adjusted based on the temporal characteristics in the study region to include those MCSs with a relative weak intensity before formation, so that the initial stage of the MCS life cycle can be detected. The tracking algorithm is able to improve the techniques to nowcast MCSs, especially once the next generation geostationary satellites such as GOES-R (Schmit et al. 2005) begin operating with a more frequent scanning schedule.

An automatic tracking algorithm using combined GEO satellite IR data and CMORPH precipitation estimate products is adopted in this study to identify and track MCS events from May to August in 2008–09 in the middle of east China. The algorithm used an areal overlap method similar to that of Schröder et al. (2009), with an improvement in the utilization of both forward and backward tracking as well as searching for precipitation associated with the identified MCSs. With this tracking strategy, the work intends to study the MCS life cycle, which includes the development period before its formation. By applying CMORPH data, more detail is provided in the evolution of both clouds and precipitation for MCSs, such as the sequence in which cloud and precipitation features occur. Results showed that the
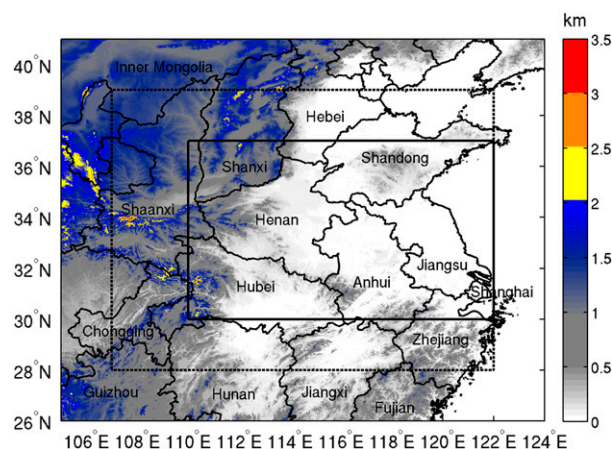

FIG. 1. Topography map of the middle of east China with the names of related provinces and municipalities. The solid box denotes the study region; the dotted box shows the buffer area for tracking MCSs.

MCSs formed most frequently in southwest Henan Province and at the border of four provinces—Shandong, Henan, Anhui, and Jiangsu—which is east of the convergence zone near the terrain's edge. Locations of the highest cloud tops and of the heaviest precipitation rates did not always match. In addition, the MCSs in the study region tended to first reach the maximum precipitation rate, followed by the minimum brightness temperature.

Section 2 introduces the method and data used to identify and track MCSs. Section 3 describes the general features of MCSs such as spatial distribution and diurnal cycle. The last section provides a summary and discussion.

2. Data and methodology

a. *MTSAT-1R satellite and CMORPH precipitation data*

MCSs from May to August in 2008 and 2009 in the middle of east China (30°–37°N, 110°–122°E, denoted by the solid inner box in Fig. 1) were examined. This area includes the Shandong, Jiangsu, Anhui, Shanghai, Hubei, and Henan provinces. This region was chosen because it has some of the most intense convection in China during the summer (Xu 2013). In addition, this region has the highest frequency of squall-line formation in east China during these two years (Meng et al. 2013). The data used in this work include the *Multifunctional Transport Satellite-1R* (*MTSAT-1R*) and CMORPH precipitation products (Joyce et al. 2004).

The MTSAT series are Japanese GEO satellites for weather and aviation applications and operations. Launched in 2006 and positioned in geostationary
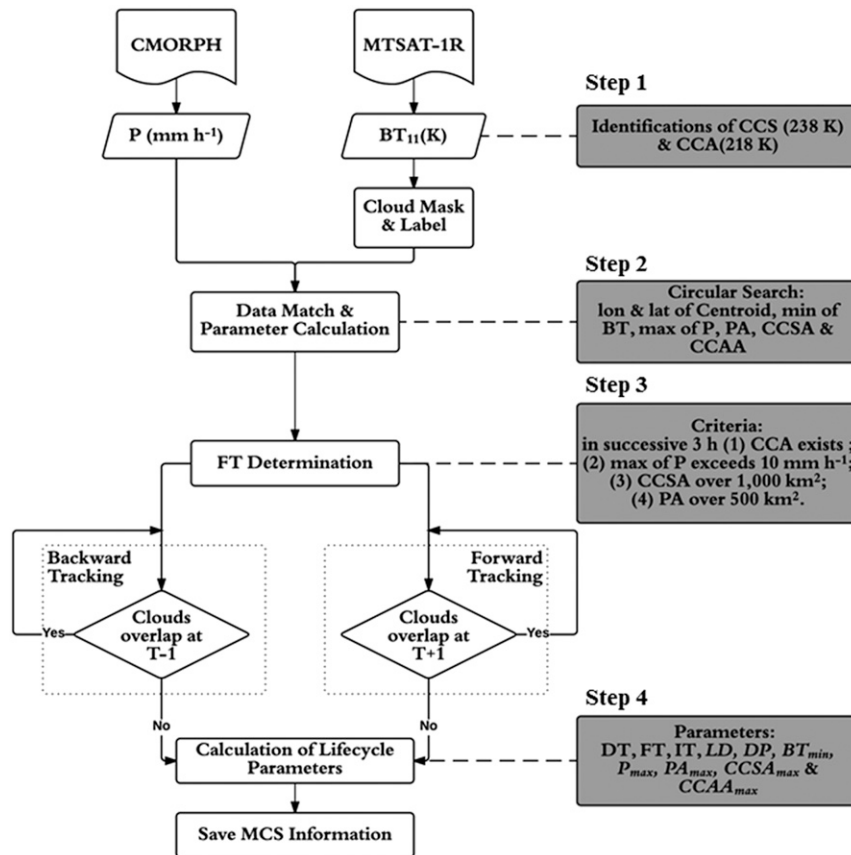
FIG. 2. Flowchart of MCS identification and tracking algorithm. Data (parallelogram), process (white boxes), decision (diamonds), and illustration (gray boxes) are presented. 1) Step 1: Cloud identification: Potential MCS clouds are labeled and classified using *MTSAT-1R* infrared channel BT based on different thresholds for each time. 2) Step 2: Matching between IR imagery and precipitation estimates: For each potential MCS, associated rain regions were matched via circular search method. 3) Step 3: Tracking MCSs: The formation time (FT) of an MCS is identified using certain criteria. Starting from FT, the convective cloud is tracked backward until its initiation and forward to the disappearance of the system or when it moves outside of the study area. 4) Step 4: MCS life cycle parameters are calculated.

orbit 35 800 km above the equator at 140°E, *MTSAT-1R* has five broadband channels covering the visible (VIS) and IR spectrum (one visible and four infrared) (http://www. jma.go.jp/jma/jma-eng/satellite/introduction/MTSAT_ series.html). The BT measurements were obtained from the MTSAT High Rate Information Transmission (HRIT) Level 1 hourly product (during the research period) with a spatial resolution of 5 km at nadir. The images were interpolated onto 0.05° grids of longitude and latitude. The BT of the 10.3–11.3-μm atmospheric window channel (with weak water vapor absorption) can well represent CTH when clouds are deep (optically thick). The large contrast between a cold cloud top and warm background makes MCSs easy to identify from IR BT images.

The CMORPH is a global precipitation analysis at high spatial and temporal resolution based exclusively

on LEO satellite microwave observations (Joyce et al. 2004). The precipitation estimates of CMORPH are derived half-hourly from LEO passive microwave observations. The observed precipitation features are propagated by motion vectors derived from GEO satellite IR data. In addition, the shape and intensity of the precipitation features are modified (morphed) during the time between microwave sensor scans by performing a time-weighted linear interpolation. Details on this technique are explained online at http://www.cpc.ncep.noaa. gov/products/janowiak/cmorph_description.html. Realtime CMORPH data are available at a resolution of about 8 km at the equator every 30 min. The product is interpolated into a grid with a grid spacing of 0.072 27° in latitude and longitude. Because of the application of GEO IR data, the temporal and spatial resolutions of

TABLE 1. Definition of parameters used in this study.

Name	Definition	Unit
CCS	MCS convective cloud system (BT < 238 K)	
CCA	MCS convective center area (BT < 218 K)	
IT	MCS initiation time, when no forerunner was found in the previous IR image	
FT	MCS formation time, when an MCS system meets formation criteria	
DT	MCS dissipation time, when P_{max} of CCS exceeds 5 mm h^{-1} for the last time	
LD	Life duration, the time between the time an MCS generates and its DT	h
DP	Developing period, the time between MCS FT and DT divided by LD and multiplied by 100%	%
BT_{min}	The min BT during lifetime	K
P_{max}	The max rain rate during lifetime	mm h^{-1}
PA_{max}	The max associated precipitation area during lifetime	km^2
$CCSA_{max}$	The max CCS area during lifetime	km^2
$CCAA_{max}$	The max CCA area during lifetime	km^2
ΔT	The time lapse between BT_{min}/P_{max}/PA_{max}/$CCSA_{max}$ and FT	h
ΔT_N	Normalized time lapse, ΔT divided by LD	

CMORPH data are finer compared to those from TRMM near-real-time data (3 h and 0.25°). Luo et al. (2013a) compared the CMORPH data with rain gauge precipitation data during mei-yu period in east China. Their study shows that the CMORPH product tends to overestimate moderate and light rainfall less than 5 mm h^{-1} and underestimate heavy precipitation larger than 10 mm h^{-1}. During their study period, they also found that CMORPH overestimates the major precipitation peak in the afternoon and underestimates the other precipitation peak in the early morning.

b. Identification of MCSs

The MCSs were identified in this work by using combined BT measurements and precipitation estimate data through the following four steps and as illustrated in Fig. 2.

1) STEP 1: CLOUD IDENTIFICATION

Similar to Mathon and Laurent (2001), clouds were first classified into two different categories: convective cloud system (CCS; BT < 238 K) (Steranka et al. 1986) and convective center area (CCA; BT < 218 K) (Machado et al. 1998) (Table 1). There is no universal threshold in BTs for MCS identification. For example, Zheng et al. (2008) used 241 K to identify meso-α convection and 221 K to identify meso-β convection in China and its neighboring regions. Mathon and Laurent (2001) categorized MCSs over Sahel with thresholds of 233 and 213 K for deep convection and the most active part of convective systems, respectively. The IR thresholds used in this work were effective in identifying the MCSs as demonstrated by an example at 1800 UTC 28 August 2008 as shown in Fig. 3. The IR imagery (Fig. 3a) reasonably matched the radar reflectivity derived from *CloudSat* and CTH from the *Cloud–Aerosol Lidar and Infrared Pathfinder Satellite Observations* (*CALIPSO*)

obtained approximately 20 min earlier (Fig. 3b). These two LEO satellites as part of NASA's Afternoon Constellation (A-Train) use active microwave measurements to observe not only the cloud tops but also the vertical structure of clouds along their paths (the straight line in Fig. 3a). It is clear that the IR thresholds used in this study are able to show the high cloud anvils of MCSs, and thus are effective in identifying the MCSs. Additionally, a slight change in the BT threshold within 5 K does not have a significant impact on our conclusions.

2) STEP 2: MATCHING IR IMAGERY WITH PRECIPITATION ESTIMATES

The rain-rate estimate for each CCS was defined as follows (illustrated in Fig. 4). We first transformed the CMORPH precipitation estimate data into hourly rain-rate estimates (mm h^{-1}) at the same time resolution of the *MTSAT-1R* BT measurements. Then a box (outlined by dashes in Fig. 4) was drawn in the IR images of every CCS bounded by the extreme latitudes and longitudes of the 238-K contour of BT (orange contour in Fig. 4). A circular searching area was plotted centered over the CCS with a radius of the maximum distance from the centroid to the four apexes of the bounding box. The precipitation estimate for the CCS was then defined as the precipitation with a rain rate larger than 1 mm h^{-1} within the circular searching area.

3) STEP 3: TRACKING MCSS

To eliminate errors caused by the boundary of the study area, a larger buffer area (the dotted box in Fig. 1) was used to track the systems. The buffer area extended northward and southward by 2°. Because the typical length of an MCS is 10–100 km, MCSs with associated precipitation at the border of the solid box should generally be covered by this buffer area. Considering the
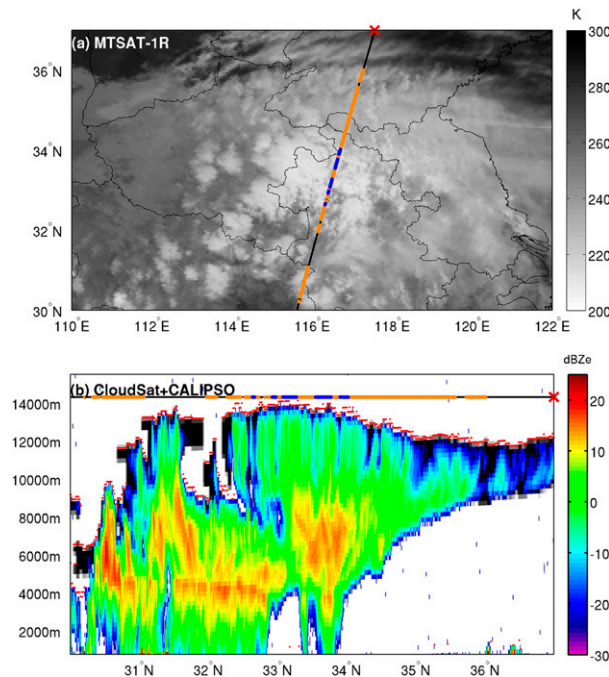
FIG. 3. Match between *CloudSat* and *CALIPSO* and IR images in the study region at 1800 UTC 28 Aug 2008. (a) Enhanced IR cloud image with the black line noting the trajectory of *CloudSat* and *CALIPSO* path and the red cross [on the upper edge of (a) and (b)] noting the starting point. The orange line in (a) denotes the range of defined MCS CCSs, and the blue line denotes the defined MCS CCAs. (b) Radar reflectivity factor and cloud (red dots) derived from *CloudSat* and *CALIPSO*. The orange line on top in (b) denotes the range of CCSs and the blue line denotes the range of CCAs.
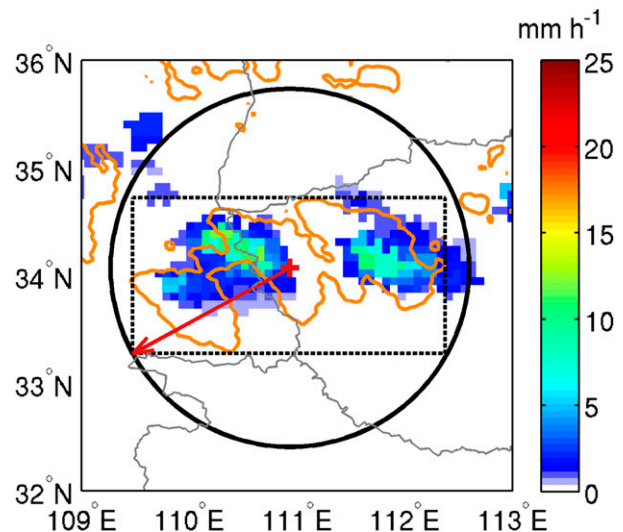

FIG. 4. Illustration of the precipitation region matched for MCS systems. MCS systems are within the orange contour of BT (238 K) identified from *MTSAT-1R* infrared BT images. The precipitation regions (described with the rain rate in mm h^{-1}) are shaded. The dark red cross (center) is the centroid of the MCS system, and the red arrow (radius) is the maximum distance from the centroid to four apexes of the bounding box (black dashed rectangle). Therefore, the circular search range (bold black circle) can be drawn to find the associated rain within the range for each MCS system.

westerly prevailing wind in the study region, the buffer area extended larger on the west than on the other sides. Since the eastern border of the solid box was already over the sea, the buffer zone was not extended on the eastern side.

Convective clouds were tracked based on an areal overlap method, similar to the one described by Schröder et al. (2009). This technique assumes that on successive satellite images, a cloud at a later time corresponds to one at an earlier time when their positions overlap (illustrated in Fig. 5). The tracking method was only applied to CCSs, because a warmer threshold could result in large systems, which actually comprise several independent small convective systems, while a colder threshold might result in excluding small systems that are developing rapidly. As Han et al. (2009) mentioned in their storm tracking algorithm, using a moderate threshold is important because a colder threshold tends to produce less overlapping, thus shortening the lifetime of MCSs and resulting in significant errors for the statistical analysis of life cycle parameters such as life duration.

An MCS was identified through a combination of satellite and precipitation information. The formation time (FT) of an MCS was determined when the following four criteria were first met in three successive hours: 1) the CCA existed, 2) the maximum rain rate exceeded 10 mm h^{-1}, 3) the area of CCS was over 1000 km^2, and 4) the total area of the precipitation region was more than 500 km^2 (Mathon and Laurent 2001). When all the criteria were met, the end of the 3-h period was defined as the FT of an MCS.

Starting from the FT, the MCS is then tracked backward until there is no forerunner in the previous image at $T-1$ (Fig. 2). The "forerunner" is the corresponding CCS in a previous image that overlaps the CCS at the current time (Fig. 5). The clouds in successive images are considered the same if the overlap covers more than 10% of the cloud area in the previous image. The smaller overlapping rate used in this study enables the tracking of small convective clouds right after convective initiation. Since MCSs in the study region usually contain multiple convective cells, if several MCSs satisfy this condition, the system with the largest overlapping area keeps the label. The MCS was then tracked forward until there was no successor in the next image ($T+1$). "Successor" is the corresponding CCS in the next image that overlaps the CCS at the current time (Fig. 5). When
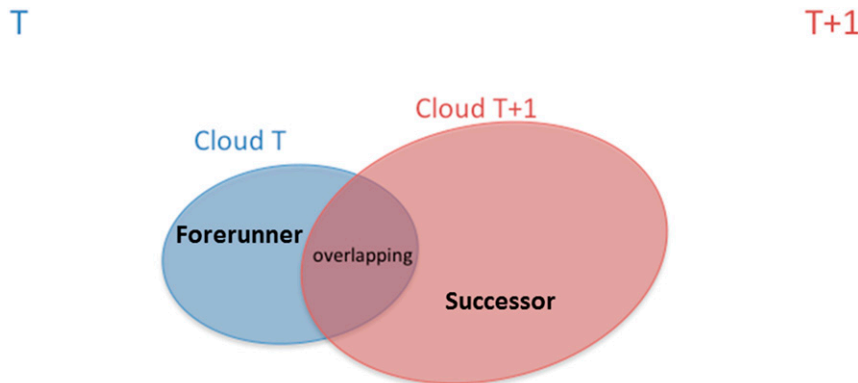
FIG. 5. Diagram showing the overlap between the cloud at T (blue shading) and $T + 1$ (pink shading) in the overlapping method. If the overlapping rate is larger than 10% (the overlap covers more than 10% of the cloud area in the previous image), the cloud at $T + 1$ is considered as the corresponding cloud at T. The cloud at T is regarded as the "forerunner" of the cloud at $T + 1$, and the cloud at $T + 1$ as the "successor" of the cloud at T.

several potential successors appear in the next image, the system with the largest overlap keeps the label. The initiation time (IT) of the MCS was defined when no forerunner was found in the previous image, while the termination of the MCS was defined at a time when no successor was found in the next image. The dissipation time (DT) of an MCS was defined when the maximum of the system's rain rate becomes lower than $5 \, \mathrm{mm \, h^{-1}}$ (Laurent et al. 2002; Yuan and Houze 2010).

4) STEP 4: CALCULATION OF MCS LIFE CYCLE PARAMETERS

Introducing the buffer zone enables the tracking of MCSs that were developing and have significant impact within the study region, but would also include some MCSs not inside the study area while still in the buffer zone. To make sure every MCS tracked is in the study region, we ruled out those events for which ⅔ of the whole lifetime were outside the study area. The life duration LD of an MCS was calculated as the time between IT (from a cloud perspective) and DT (from a precipitation perspective). The developing period DP of an MCS is the time between IT and FT divided by LD and multiplied by 100%:

$$\mathrm{DP} = \frac{(\mathrm{FT} - \mathrm{IT})}{\mathrm{LD}} \times 100\% . \tag{1}$$

The LD and DP for each MCS event, as well as the minimum BT ($\mathrm{BT_{min}}$), the maximum rain rate ($P_{\max}$), the maximum associated precipitation area ($\mathrm{PA_{max}}$), the maximum CCS area ($\mathrm{CCSA_{max}}$) and the maximum CCA area ($\mathrm{CCAA_{max}}$) during MCS life cycle were examined. Here $\mathrm{BT_{min}}$, $P_{\max}$, $\mathrm{PA_{max}}$, and $\mathrm{CCSA_{max}}$ are the four parameters that describe the convective intensity of MCSs also used in other studies (e.g., Feng et al. 2012; Xu 2013). Physically, the strength of convective updrafts could be indicated by $\mathrm{BT_{min}}$: the smaller the $\mathrm{BT_{min}}$ is, the higher the cloud top will be. Here $P_{\max}$ is the parameter for the heaviest precipitation, and $\mathrm{PA_{max}}$ represents the largest area covered by an MCS. Both $\mathrm{CCSA_{max}}$ and $\mathrm{CCAA_{max}}$ denote the size of the highest part of the cloud tops, with larger values indicating more moisture and energy transferred from near the surface to the tropopause. The term $\mathrm{CCAA_{max}}$ represents the size of the most active part of the convection, usually having a stronger moisture and energy exchange than $\mathrm{CCSA_{max}}$. Previous studies show that inside an MCS strong convective activity is usually associated with intense precipitation (described by $P_{\max}$) resulting from a rapid vertical updraft (indicated by $\mathrm{BT_{min}}$) and followed by an expanding anvil cloud (by $\mathrm{CCSA_{max}}$ and $\mathrm{CCAA_{max}}$) (Houze 2004; Mathon and Laurent 2001; Schröder et al. 2009). The distributions of time lapse and normalized time lapse of the four parameters with respect to FT were calculated to analyze MCS diurnal cycles in the study region.

3. General features of the identified MCSs

a. Geographical distribution of MCS formation and dissipation

A total of 280 MCS events were identified and tracked between 1 May and 31 August in 2008–09. MCS formation was concentrated in southwest Henan Province and near the border of four provinces including Shandong, Henan, Anhui, and Jiangsu (Fig. 6a). This result is consistent with Meng et al. (2013), which found that the maximum frequency of squall lines was located
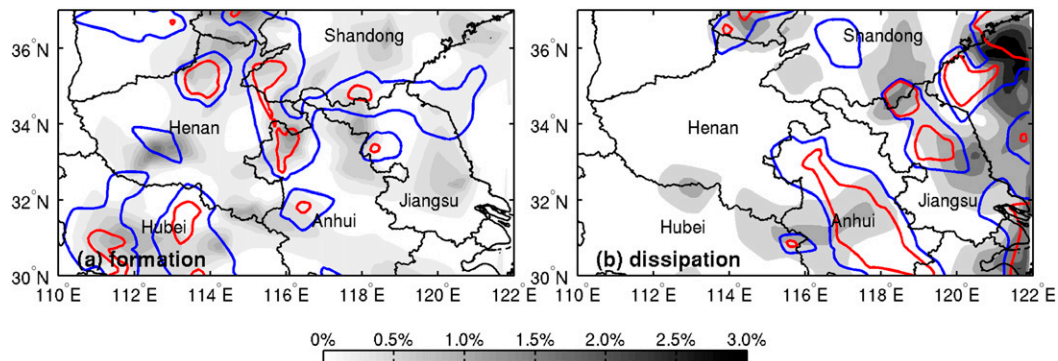
FIG. 6. The frequency of MCS (a) formation and (b) dissipation in the study area: The shading areas show the positions of cloud tops. The blue and red contour lines denote where frequencies of MCS formation and dissipation are over 0.5% and 1.0% for the most intense precipitation, respectively.

between the borders of the same four provinces. The centroids of cloud tops and the strongest precipitation of MCSs were at different locations (Fig. 6). The strongest precipitation (contoured in Fig. 6) does not always overlap with the cloud tops, which suggests the necessity of tracking an MCS based on the evolution of not only the cloud tops but also its precipitation. The maximum frequency of MCS dissipation in terms of the cloud top was observed near the eastern edge of the box (Fig. 6b). Similar to the formation, the location of the maximum frequency of the cloud tops was different from that of the precipitation. The highest frequency of the heaviest precipitation was observed not only at the same location as that of cloud top, but also over land between Shandong and Jiangsu Provinces and in Anhui Province.

The boundary among the four provinces is located in the Yangtze and Huai River basin in east China where low-level vortices originating from the Tibetan Plateau or Sichuan basin are quite frequent and favorable for the formation of convective systems (Yasunari and Miwa 2006; Fujinami and Yasunari 2009). Its flatness and frequent large-scale low-level convergence in association with surface fronts are also favorable for the enhancement of convective storms (Luo et al. 2013b). MCSs frequently form east of the terrain over the plain territories according to Fig. 1. One possible explanation is that convection is triggered when organized horizontal convergence (shown in Fig. 7) occurring near the edge of the topographical elevation, like mountains, coincides with high CAPE and low CIN (Barthlott and Kirshbaum 2013). Based on the results above, an obvious eastward propagation trend between MCS formation and dissipation was observed in the study region, which is consistent with Xu and Zipser (2011). According to previous studies, the westerly steering winds between 300 and 500 hPa are a major contributor to the propagation pattern during the monsoon period from mid-May

to August, which accounts for most of our study period (Murakami and Ding 1982; Chen 1993; Lau and Yang 1997; Xu 2011).

b. Distribution of cloud and precipitation parameters

The distribution of BT_{min} (Fig. 8a) showed that over 80% of the MCSs reached a BT_{min} less than 210 K with an average of 201 K, which is consistent with the study of Xu and Zipser (2011) using TRMM data. Similarly over midlatitude, approximately 90% of the convective systems over the central United States from the study of Feng et al. (2012) have a minimum cloud-top brightness temperature lower than 220 K. Compared with MCSs in tropical regions with a typical BT_{min} of less than 200 K (Mathon and Laurent 2001; Goyens et al. 2012), MCSs in midlatitudes as in this study area are less deep (lower cloud tops and higher BTs), which is likely because the height of the tropopause in the tropics is considerably higher than that in the midlatitudes.

The mean of P_{max} was 28 mm h^{-1}, and over half of the cases experienced a maximum rain rate over 20 mm h^{-1} (Fig. 8b). The P_{max} features of the MCSs have not been examined in previous studies since all previously available satellite precipitation estimates were obtained from daily rain accumulation (e.g., Fiolleau and Roca 2013) or near-real-time satellite product like TRMM 3B42 (e.g., Goyens et al. 2012). The temporal and spatial resolution of those satellite products were quite coarse, and thus could not provide precipitation variation features during the MCS life cycle.

The LD had a lognormal distribution (Fig. 8c) with an average value of 20.8 h. About 75% of the events lasted over 5 h, and about 40% lasted over 24 h. The mean LD in this study was longer than that found in Feng et al. (2012) (shorter than 14 h), Laing and Fritsch (1997) (10 h), and Velasco and Fritsch (1987) (9.5 h). The tracking method applied in our study used a smaller overlapping rate
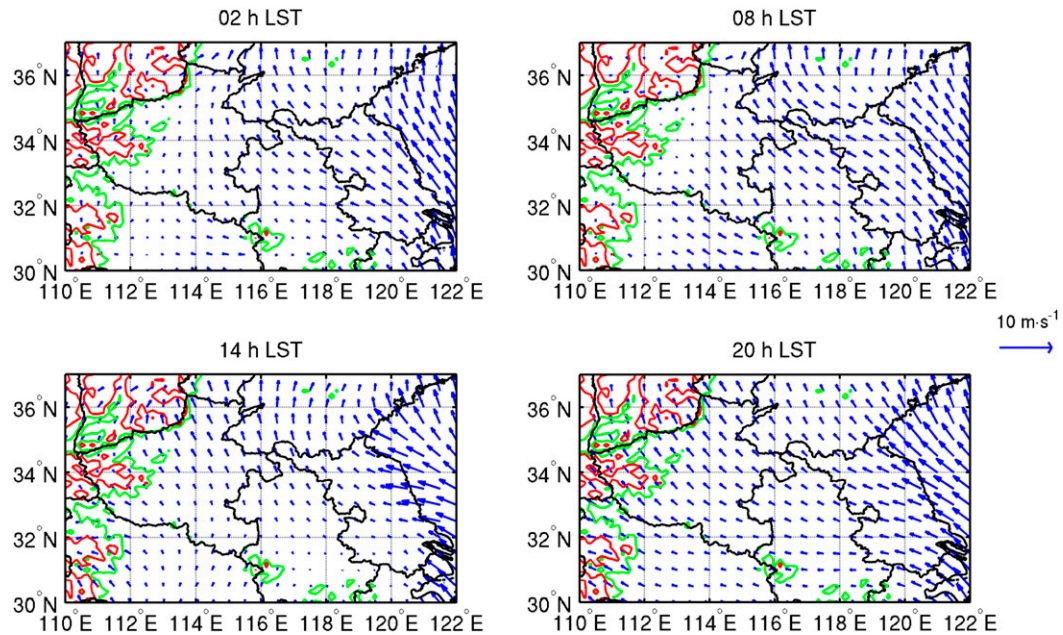
FIG. 7. The 10-m wind during May–August 2008–09. The green and red contour lines represent the topographic elevation of 500 and 1000 m, respectively.

(10%) due to the 1-h temporal resolution of IR imagery [while Feng et al. (2012) used a 50% overlap rate with 30-min GOES imagery], which contributes to a longer LD than MCSs over the United States. Additionally, Laing and Fritsch (1997) and Velasco and Fritsch (1987) used larger cutoff cloud areas to shorten the life duration of the MCSs in their study.

In Fig. 8d, DP shows a mean value of 55.5%, and 80% of the events spent over 1/5 of their lifetime in development. As a result of a smaller overlapping rate, the average tracking duration between IT and FT is about 10 h. The period 10 h ahead of the formation peak (in section 3c) is around 8 h local standard time (LST, UTC + 8) when the convergence shown by 10-m wind (Fig. 7) is the strongest, which indicates the high possibility of convective initiation. Compared to previous studies that tracked MCSs by radar, tracking MCSs with GEO satellites is able to detect the potential convection before precipitation starts, which can improve the nowcasting of MCSs.

The PA_{max} exhibited an exponential distribution (Fig. 8e) and most events had PA_{max} slightly over 10^4 km^2, with an expected value of 5.2×10^4 km^2. This result is consistent with the area of precipitation within MCSs from Xu and Zipser (2011) using TRMM data, and is on the same scale as convective systems in the central United States (Feng et al. 2012). However, because of the overestimating of moderate and light rainfall by CMORPH, the result of PA_{max} may be overestimated slightly since

the rain rate where smaller than 1 mm h^{-1} is not included for calculation. $CCSA_{max}$ had a Weibull distribution (Fig. 8f) with a major peak of 10^5 km^2 and a mean value of 1.8×10^5 km^2, which were both about the same scale as Maddox's definition of MCSs (Maddox 1980), but smaller than average MCSs over tropical land (Mathon and Laurent 2001; Goyens et al. 2012). $CCAA_{max}$ also showed a Weibull distribution (Fig. 8g), mainly ranging between 10^4 and 10^5 km^2 with an expected average value of 5.3×10^4 km^2. The shape parameter of a Weibull distribution could describe the extreme value distribution. The distribution in this study indicates that MCSs of small and moderate sizes are more common, while those of large sizes are relatively rare.

c. Diurnal cycle of MCS formation and dissipation, and occurring sequences of cloud, precipitation, and MCS features

The diurnal cycle of MCSs is closely associated with the diurnal variation of precipitation during warm seasons (Lin et al. 2000; Liang et al. 2004). It shows the climatic characteristics of the study region and is often regarded as the basis for the regional forecasting of MCSs including its precipitation. The FT of MCSs tracked in our study showed two peaks, similar to many midlatitude areas (Hamilton 1981; Dai 2001; Tian et al. 2005; Chen et al. 2009). The major peak was in the late afternoon and early evening around 1800 LST when strengthening CAPE occurs after 1400 LST (Dai 2001);
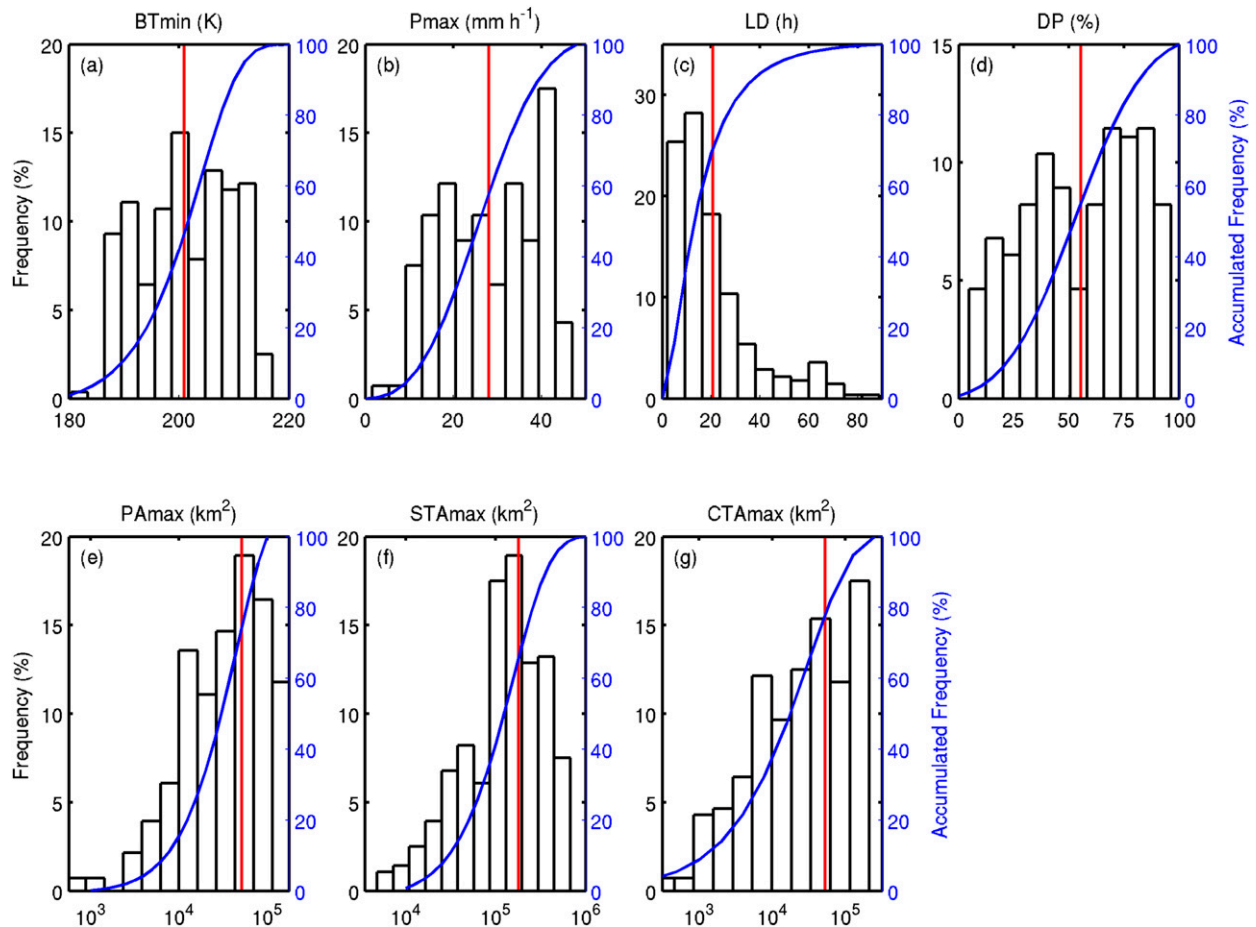
FIG. 8. Distributions (bars) and fitted cumulative distribution functions (blue lines) of the cloud and precipitation variables: BT_{min}, P_{max}, LD, DP, PA_{max}, $CCSA_{max}$, and $CCAA_{max}$ in the warm season between 2008 and 2009. The red vertical lines mark the mean values of each variable.

and the minor peak was in the early morning around 0600 LST, which is associated with a wavelike propagation of afternoon convection, mountain–plain circulation, and nocturnal low-level jets (Yu et al. 2007; Huang et al. 2010; Xu and Zipser 2011). The convection formed during the morning peak is less deep (warmer BT_{min}) as Xu and Zipser (2011) found with TRMM data and also with a smaller LD and $CCSA_{max}$ (not shown). The two-peak pattern of the MCS formation is consistent with the results by Zheng et al. (2008) and Meng et al. (2013). The diurnal cycle is also very similar to the precipitation diurnal cycle in east China observed by Yu et al. (2007) with rain gauge records and Dai (2001) with global weather reports. As an MCS dissipates after its maturity, it also has two peaks (Fig. 9). The most likely period for MCS decay was in the morning after sunrise around 0900 LST when CAPE is at its lowest during the day for east China (Dai 2001), similar to that found in Laing and Fritsch (1997). The second peak is around

0300 LST as CAPE decreases significantly after reaching its maximum before midnight, which is especially significant in the eastern portion of the study region (Dai 2001). The least likely period for decay was in the afternoon when convective initiation was most likely.

The diurnal distributions of BT_{min}, P_{max}, PA_{max}, and $CCSA_{max}$ had a similar peak in the late afternoon around 1800 LST (Fig. 10a), which was similar to that found in Feng et al. (2012) for MCSs over the southern Great Plains (SGP) in the United States. The diurnal cycle of P_{max} has a secondary peak in the early morning around 0600 LST, which is consistent with the observation by Dai (2001) and Yu et al. (2007). The PA_{max}, however, occurs least frequently around 2100 LST while P_{max} occurs most frequently during this period. Around midnight the P_{max} frequency decreased while the PA_{max} frequency increased. It can be inferred from this result that convective precipitation occurs more frequently in MCSs around 2100 than 0000 LST when the stratiform
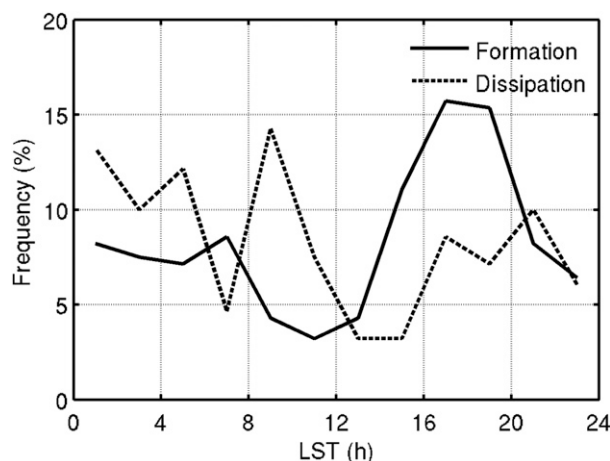
FIG. 9. Diurnal distribution of MCS formation and dissipation times (in LST, UTC + 8).

precipitation portion grows. The diurnal variations in BT_{min} and $CCSA_{max}$ are almost of the same phase and have larger variations in amplitude than P_{max} and PA_{max}.

The time sequence in which the four parameters BT_{min}, P_{max}, PA_{max}, and $CCSA_{max}$ occur was examined in terms of the difference between the occurrence of the four parameters (T_m) and FT: $\Delta T = T_m - FT$. Among half of the events, ΔT s of all the four parameters were within 5 h after FT (Fig. 10b). This result was similar to that found by Feng et al. (2012) (3–6 h) for BT_{min} and P_{max} of the MCSs in central United States. It is also shown in Fig. 10b that the ΔTs of BT_{min} and P_{max} in this study were about 2 h earlier than that of the two areal variables. This result was reasonable considering that strong convective activity is usually associated with intense precipitation resulting from a rapid vertical updraft and followed by an expanding anvil cloud (Houze 2004; Mathon and Laurent 2001; Schröder et al. 2009). Therefore, the peak in precipitation should be preceded by a minimum in BT (representing strong vertical updraft) and followed by a maximum in cloud coverage, which is observed by Pope et al. (2008) over northern Australia.

To show the sequence in which the four parameters occurs more clearly, a normalized time lapse ΔT_N was calculated by dividing ΔT by LD (Fig. 10c). Results showed that the normalized time lapses of BT_{min} and P_{max} were very close to each other, while P_{max} appeared slightly earlier than BT_{min}. The occurrence of P_{max} ahead of BT_{min} in MCSs over east China is opposite to what was observed in a single cell (Houze 2004) likely due to their multicell structures. The situation is much more complicated when multiple cells coexist, which are quite common for MCSs over China (Chen et al. 2012; Meng et al. 2013). Inside a multicell convective system,
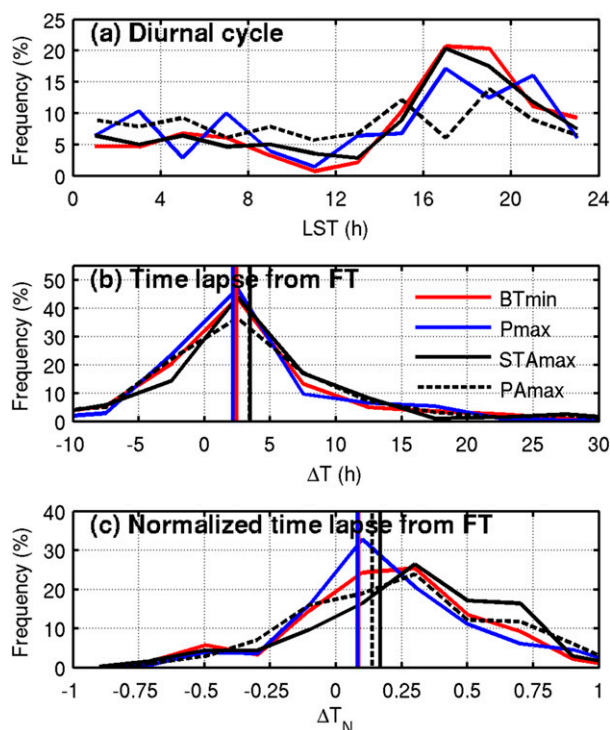

FIG. 10. (a) Diurnal cycle of the four MCS parameters: BT_{min}, P_{max}, $CCSA_{max}$, and PA_{max}. (b) Frequency distribution of the time lapse (h) between MCS formation and the four MCS parameters; and (c) the time lapse according to the normalized lifetime. Vertical lines in (b) and (c) denote the mean (normalized) time lapse of the four MCS parameters.

the precipitation of several convective cores might connect into one contiguous rain area as observed by Yuan and Houze (2010). The updraft of this whole system may continue to grow after the precipitation reaches its maximum. Under this circumstance, the moisture is no longer sufficient while the dynamic condition is still favorable for convective development. It may also result from the merging of a new system with an ascending cloud top but weaker precipitation. Results also showed that the time lapse of PA_{max} occurred ahead of that of $CCSA_{max}$. A possible reason could be that the MCS anvil continues extending when the rain starts to decline, or the nonprecipitation anvil dominates (Yuan and Houze 2010).

4. Summary and future work

With IR images from Japan's *MTSAT-1R* satellite and CMORPH precipitation estimate data, a method that can identify and automatically track MCSs was developed and used to perform a statistical analysis on MCSs in the warm season from May to August of 2008 and 2009 over the middle of east China. This methodology is adjusted to

include those MCSs with a relative weak intensity before formation. The unique advantage of combining high temporal and spatial resolution geostationary satellite brightness temperature images and precipitation measurements for tracking MCSs is that the CTH along with the coverage and the precipitation intensity can be well identified.

A total of 280 MCS events were identified and tracked. Southwest Henan Province and the border of four provinces—Shandong, Henan, Anhui, and Jiangsu—were the most frequent regions for MCSs to form, which is east of the convergence zone near the terrain's edge. In the dissipation stage, the cloud tops generally had already moved over the East China Sea, while a proportion of the largest precipitation rates still remained over land. Results showed that the location of the highest cloud tops and the heaviest rain rates did not always match, which shows the advantage of the tracking algorithm combining both cloud tops and precipitation. MCS locations and eastward propagation in this study are consistent with the analysis of the East Asia monsoon and terrain impact (Murakami and Ding 1982; Xu and Zipser 2011; Luo et al. 2013b).

The intensity parameters of MCSs in China are very similar compared to MCSs in the United States; 75% of the MCSs lasted over 5 h. The longer life duration in this study is due to a tracking method with a smaller overlapping rate compared to previous studies, which includes the rapid development period after convective initiation and before MCS formation. As a result, a relatively longer DP is observed in this study, indicating the potential of improving MCS nowcasting via GEO satellite observations.

The diurnal cycle of the identified MCSs showed two peaks in formation frequency, slightly different from MCSs in the United States due to the difference in the diurnal variation pattern of CAPE. Four parameters that describe the convective intensity of the identified MCSs were examined, including the minimum BT, the maximum precipitation rate, the maximum convective system area, and the maximum associated precipitation area. The parameters of about half the MCSs turned to their maximum or minimum within 5 h after formation. MCSs over east China tended to reach the maximum rain rate first, followed soon after by the appearance of minimum BT, then the maximum precipitation area, and finally the maximum MCS system area. It is the multiple-cell structures of MCSs that bring more complicated results in the sequence of the convective intensity parameters.

Future work will focus on combining GEO satellite data and LEO satellite data with active remote sensing. The next-generation imagers on board GEO satellites such as the newly launched *Himawari-8* and GOES-R to be launched in 2016 (Schmit et al. 2005; Kurino 2012), will provide more bands and more frequent scans to monitor the life cycles of MCSs. Active remote sensing measurements on board LEO satellites will give more information on the cloud parameters, including the cloud structure, inner flow, precipitation, and anvils. Thus, a study that includes active remote sensing data from satellite and makes comparisons between the results concluded from both active and passive satellite observations and ground-based radar analysis will help reveal the internal structure of MCSs and show more precise life cycles of multiple-cell MCSs in different organizational modes.

REFERENCES

Barthlott, C., and D. J. Kirshbaum, 2013: Sensitivity of deep convection to terrain forcing over Mediterranean islands. *Quart. J. Roy. Meteor. Soc.*, **139**, 1762–1779, doi:10.1002/qj.2089.

Bei, N., S. Zhao, and S. Gao, 2002: Numerical simulation of a heavy rainfall event in China during July 1998. *Meteor. Atmos. Phys.*, **80**, 153–164, doi:10.1007/s007030200022.

Chen, H., T. Zhou, R. Yu, and J. Li, 2009: Summer rain fall duration and its diurnal cycle over the U.S. Great Plains. *Int. J. Climatol.*, **29**, 1515–1519, doi:10.1002/joc.1806.

Chen, M., Y. Wang, F. Gao, and X. Xiao, 2012: Diurnal variations in convective storm activity over contiguous North China during the warm season based on radar mosaic climatology. *J. Geophys. Res.*, **117**, D20115, doi:10.1029/2012JD018158.

Chen, Y.-L., 1993: Some synoptic-scale aspects of the surface fronts over southern China during TAMEX. *Mon. Wea. Rev.*, **121**, 50–64, doi:10.1175/1520-0493(1993)121<0050:SSSAOT>2.0.CO;2.

Dai, A., 2001: Global precipitation and thunderstorm frequencies. Part II: Diurnal variations. *J. Climate*, **14**, 1112–1128, doi:10.1175/1520-0442(2001)014<1112:GPATFP>2.0.CO;2.

Feng, Z., X. Dong, B. Xi, S. A. McFarlane, A. Kennedy, B. Lin, and P. Minnis, 2012: Life cycle of midlatitude deep convective systems in a Lagrangian framework. *J. Geophys. Res.*, **117**, D23201, doi:10.1029/2012JD018362.

Fiolleau, T., and R. Roca, 2013: Composite life cycle of tropical mesoscale convective systems from geostationary and low earth orbit satellite observations: Method and sampling considerations. *Quart. J. Roy. Meteor. Soc.*, **139**, 941–953, doi:10.1002/qj.2174.

Fujinami, H., and T. Yasunari, 2009: The effects of midlatitude waves over and around the Tibetan Plateau on submonthly variability of the East Asian summer monsoon. *Mon. Wea. Rev.*, **137**, 2286–2304, doi:10.1175/2009MWR2826.1.

Goyens, C., D. Lauwaet, M. Schröder, M. Demuzere, and N. P. Van Lipzig, 2012: Tracking mesoscale convective systems in the Sahel: Relation between cloud parameters and precipitation. *Int. J. Climatol.*, **32**, 1921–1934, doi:10.1002/joc.2407.

Hamilton, K., 1981: A note on the observed diurnal and semi-diurnal rainfall variations. *J. Geophys. Res.*, **86**, 12 122–12 126, doi:10.1029/JC086iC12p12122.

Han, L., S. Fu, L. Zhao, Y. Zheng, H. Wang, and Y. Lin, 2009: 3D convective storm identification, tracking, and forecasting—An enhanced TITAN algorithm. *J. Atmos. Oceanic Technol.*, **26**, 719–732, doi:10.1175/2008JTECHA1084.1.

Houze, R. A., 2004: Mesoscale convective systems. *Rev. Geophys.*, **42**, RG4003, doi:10.1029/2004RG000150.

Huang, H.-L., C.-C. Wang, G. T.-J. Chen, and R. E. Carbone, 2010: The role of diurnal solenoidal circulation on propagating rainfall episodes near the eastern Tibetan Plateau. *Mon. Wea. Rev.*, **138**, 2975–2989, doi:10.1175/2010MWR3225.1.

Joyce, R. J., J. E. Janowiak, P. A. Arkin, and P. Xie, 2004: CMORPH: A method that produces global precipitation estimates from passive microwave and infrared data at high spatial and temporal resolution. *J. Hydrometeor.*, **5**, 487–503, doi:10.1175/1525-7541(2004)005<0487:CAMTPG>2.0.CO;2.

Kolios, S., and H. Feidas, 2013: An automated nowcasting system of mesoscale convective systems for the Mediterranean basin using Meteosat imagery. Part I: System description. *Meteor. Appl.*, **20**, 287–295, doi:10.1002/met.1282.

Kurino, T., 2012: Future plan and recent activities for the Japanese Follow-on Geostationary Meteorological Satellite *Himawari-8/9*. *Fall Meeting 2012*, San Francisco, CA, Amer. Geophys. Union, Abstract IN43E-03.

Laing, A. G., and J. M. Fritsch, 1997: The global population of mesoscale convective complexes. *Quart. J. Roy. Meteor. Soc.*, **123**, 389–405, doi:10.1002/qj.49712353807.

——, and ——, 2000: The large-scale environments of the global populations of mesoscale convective complexes. *Mon. Wea. Rev.*, **128**, 2756–2776, doi:10.1175/1520-0493(2000)128<2756:TLSEOT>2.0.CO;2.

Lau, K., and S. Yang, 1997: Climatology and interannual variability of the Southeast Asian summer monsoon. *Adv. Atmos. Sci.*, **14**, 141–162, doi:10.1007/s00376-997-0016-y.

Laurent, H., L. A. T. Machado, C. A. Morales, and L. Durieux, 2002: Characteristics of the Amazonian mesoscale convective systems observed from satellite and radar during the WETAMC/LBA experiment. *J. Geophys. Res.*, **107**, 8054, doi:10.1029/2001JD000337.

LeMone, M. A., E. J. Zipser, and S. B. Trier, 1998: The role of environmental shear and thermodynamic conditions in determining the structure and evolution of mesoscale convective systems during TOGA COARE. *J. Atmos. Sci.*, **55**, 3493–3518, doi:10.1175/1520-0469(1998)055<3493:TROESA>2.0.CO;2.

Liang, X.-Z., L. Li, A. Dai, and K. E. Kunkel, 2004: Regional climate model simulation of summer precipitation diurnal cycle over the United States. *Geophys. Res. Lett.*, **31**, L24208, doi:10.1029/2004GL021054.

Lin, X., D. A. Randall, and L. D. Fowler, 2000: Diurnal variability of the hydrologic cycle and radiative fluxes: Comparisons between observations and a GCM. *J. Climate*, **13**, 4159–4179, doi:10.1175/1520-0442(2000)013<4159:DVOTHC>2.0.CO;2.

Luo, Y., W. Qian, R. Zhang, and D.-L. Zhang, 2013a: Gridded hourly precipitation analysis from high-density rain gauge network over the Yangtze–Huai Rivers basin during the 2007 mei-yu season and comparison with CMORPH. *J. Hydrometeor.*, **14**, 1243–1258, doi:10.1175/JHM-D-12-0133.1.

——, H. Wang, R. Zhang, W. Qian, and Z. Luo, 2013b: Comparison of rainfall characteristics and convective properties of monsoon precipitation systems over south China and the Yangtze and Huai River basin. *J. Climate*, **26**, 110–132, doi:10.1175/JCLI-D-12-00100.1.

Machado, L., W. Rossow, R. Guedes, and A. Walker, 1998: Life cycle variations of mesoscale convective systems over the Americas. *Mon. Wea. Rev.*, **126**, 1630–1654, doi:10.1175/1520-0493(1998)126<1630:LCVOMC>2.0.CO;2.

Maddox, R. A., 1980: Meoscale convective complexes. *Bull. Amer. Meteor. Soc.*, **61**, 1374–1387, doi:10.1175/1520-0477(1980)061<1374:MCC>2.0.CO;2.

Mathon, V., and H. Laurent, 2001: Life cycle of Sahelian mesoscale convective cloud systems. *Quart. J. Roy. Meteor. Soc.*, **127**, 377–406, doi:10.1002/qj.49712757208.

Meisner, B. N., and P. A. Arkin, 1987: Spatial and annual variations in the diurnal cycle of large-scale tropical convective cloudiness and precipitation. *Mon. Wea. Rev.*, **115**, 2009–2032, doi:10.1175/1520-0493(1987)115<2009:SAAVIT>2.0.CO;2.

Meng, Z., D. Yan, and Y. Zhang, 2013: General features of squall lines in east China. *Mon. Wea. Rev.*, **141**, 1629–1647, doi:10.1175/MWR-D-12-00208.1.

Migliorini, S., M. Dixon, R. Bannister, and S. Ballard, 2011: Ensemble prediction for nowcasting with a convection-permitting model—I: Description of the system and the impact of radar-derived surface precipitation rates. *Tellus*, **63A**, 468–496, doi:10.1111/j.1600-0870.2010.00503.x.

Murakami, T., and Y. Ding, 1982: Wind and temperature changes over Eurasia during the early summer of 1979. *J. Meteor. Soc. Japan*, **60**, 183–196.

Pope, M., C. Jakob, and M. J. Reeder, 2008: Convective systems of the north Australian monsoon. *J. Climate*, **21**, 5091–5112, doi:10.1175/2008JCLI2304.1.

Schmit, T. J., M. M. Gunshor, W. P. Menzel, J. J. Gurka, J. Li, and A. S. Bachmeier, 2005: Introducing the next-generation advanced baseline imager on GOES-R. *Bull. Amer. Meteor. Soc.*, **86**, 1079–1096, doi:10.1175/BAMS-86-8-1079.

Schröder, M., M. König, and J. Schmetz, 2009: Deep convection observed by the Spinning Enhanced Visible and Infrared Imager on board Meteosat 8: Spatial distribution and temporal evolution over Africa in summer and winter 2006. *J. Geophys. Res.*, **114**, D05109, doi:10.1029/2008JD010653.

Steranka, J., E. B. Rodgers, and R. C. Gentry, 1986: The relationship between satellite measured convective bursts and tropical cyclone intensification. *Mon. Wea. Rev.*, **114**, 1539–1546, doi:10.1175/1520-0493(1986)114<1539:TRBSMC>2.0.CO;2.

Sun, J., S. Zhao, G. Xu, and Q. Meng, 2010: Study on a mesoscale convective vortex causing heavy rainfall during the mei-yu season in 2003. *Adv. Atmos. Sci.*, **27**, 1193–1209, doi:10.1007/s00376-009-9156-6.

Tian, B., I. M. Held, N.-C. Lau, and B. J. Soden, 2005: Diurnal cycle of summertime deep convection over North America: A satellite perspective. *J. Geophys. Res.*, **110**, D08108, doi:10.1029/2004JD005275.

Velasco, I., and J. M. Fritsch, 1987: Mesoscale convective complexes in the Americas. *J. Geophys. Res.*, **92**, 9591–9613, doi:10.1029/JD092iD08p09591.

Vila, D. A., L. A. T. Machado, H. Laurent, and I. Velasco, 2008: Forecast and Tracking the Evolution of Cloud Clusters (ForTraCC) using satellite infrared imagery: Methodology and validation. *Wea. Forecasting*, **23**, 233–245, doi:10.1175/2007WAF2006121.1.

Xu, W., 2011: East Asian summer monsoon precipitation systems: Rainfall characteristics, storm morphologies and convective properties. Ph.D. thesis, University of Utah, 293 pp.

——, 2013: Precipitation and convective characteristics of summer deep convection over East Asia observed by TRMM. *Mon. Wea. Rev.*, **141**, 1577–1592, doi:10.1175/MWR-D-12-00177.1.

——, and E. J. Zipser, 2011: Diurnal variations of precipitation, deep convection, and lightning over and east of the eastern Tibetan Plateau. *J. Climate*, **24**, 448–465, doi:10.1175/2010JCLI3719.1.

Yasunari, T., and T. Miwa, 2006: Convective cloud systems over the Tibetan Plateau and their impact on meso-scale disturbances in the meiyu/baiu frontal zone—A case study in 1998. *J. Meteor. Soc. Japan*, **84**, 783–803, doi:10.2151/jmsj.84.783.

Yu, R., T. Zhou, A. Xiong, Y. Zhu, and J. Li, 2007: Diurnal variations of summer precipitation over contiguous China. *Geophys. Res. Lett.*, **34**, L01704, doi:10.1029/2006GL028129.

——, W. Yuan, J. Li, and Y. Fu, 2010: Diurnal phase of late-night against late-afternoon of stratiform and convective precipitation in summer southern contiguous China. *Climate Dyn.*, **35**, 567–576, doi:10.1007/s00382-009-0568-x.

Yuan, J., and R. A. Houze, 2010: Global variability of mesoscale convective system anvil structure from A-Train satellite data. *J. Climate*, **23**, 5864–5888, doi:10.1175/2010JCLI3671.1.

Zhang, G. J., 2003: Roles of tropospheric and boundary layer forcing in the diurnal cycle of convection in the U.S. Southern Great Plains. *Geophys. Res. Lett.*, **30**, 2281, doi:10.1029/2003GL018554.

Zheng, L., J. Sun, X. Zhang, and C. Liu, 2013: Organizational modes of mesoscale convective systems over central east China. *Wea. Forecasting*, **28**, 1081–1098, doi:10.1175/WAF-D-12-00088.1.

Zheng, Y., J. Chen, and P. Zhu, 2008: Climatological distribution and diurnal variation of mesoscale convective systems over China and its vicinity during summer. *Chin. Sci. Bull.*, **53** (10), 1574–1586.